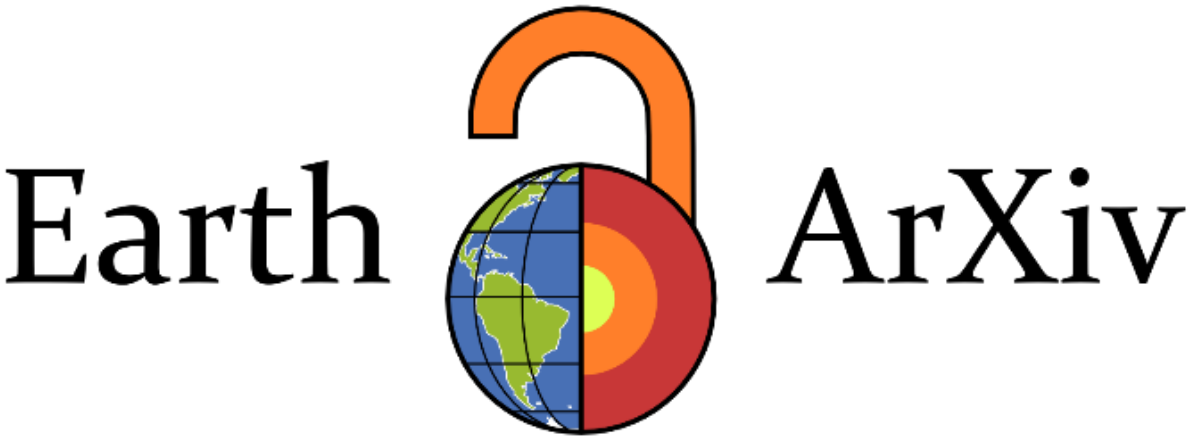

Open-source GIS-Based Multi-Criteria Flood Risk Model for data-constrained environments

Shamsudeen Abubakar,
University of Louisville

Samuel Oyatoye,
Texas Tech University

Oreoluwa Adebayo,
WeCollect

Chidumebi Ezenwoko,
California State University

Ayomide Owoyemi,
University of Illinois, Chicago

Ben Seun Oyajumo,
Obafemi Awolowo University

Joshua Owoyemi,
ModAstera, Inc. Tokyo, Japan

Favour Chiemerie Madubuko,
Ashesi University

Kelvin Akyea,
University of Cape Coast

Afeez Mohammed,
Obafemi Awolowo University

Godwin Musa,
University of Ilorin

Chisom Rutherford,
University of Calabar

Emmanuella Nkanang,
Covenant University

Kabir Mumuni,
Lagos State University

Abstract

Flooding poses a major hazard across diverse environments and can be particularly difficult to estimate in urban/urbanizing cities without detailed hydrodynamic data/models. This paper presents a GIS-based, multi-criteria model that integrates openly available hydrological, soil, land cover, and drainage network data to produce a relative Flood Risk Index (FRI) at high spatial resolution. A modular Python-based workflow is developed to fetch these data, pre-process spatial layers, normalize heterogeneous indicators, and combine them into a single 0–1 flood risk score. The model emphasizes transparency, reproducibility, and adaptability for risk screening and decision-support in flood-prone, data-scarce regions, and is demonstrated through application on several major Sub-Saharan cities. The overall product is an adaptable, extensible product to provide flood risk guidance to individuals and city planners.

Keywords: Flood risk assessment, Geographic Information Systems (GIS), Raster-based multi-criteria analysis, open-source geospatial modeling, Flood susceptibility

1. Introduction

Urban flooding is increasingly exacerbated by the combined effects of climate variability, rapid land-use change, and insufficient drainage infrastructure, particularly in fast-growing cities across the Global South. Intensifying rainfall extremes linked to climate change have increased the frequency and severity of pluvial flooding events, while unplanned urban expansion has amplified surface runoff through the proliferation of impervious surfaces and the encroachment of settlements into natural floodplains (IPCC, 2022; Di Baldassarre et al., 2017). In Sub-Saharan Africa, these pressures are especially pronounced due to high urbanization rates, limited infrastructure investment, and governance constraints that hinder effective flood risk management (Douglas et al., 2008; Adelekan, 2016).

In much of Sub-Saharan Africa, conventional flood risk assessment methods remain difficult to operationalize for routine planning. Physically based hydrodynamic models require high-resolution topography, long and reliable hydro-meteorological records, calibrated hydraulic parameters, and substantial computational resources. Although these models are increasingly being produced for the region, the conditions needed to create the mdoels are rarely/not-easily met in data-scarce and rapidly urbanizing settings (Merz et al., 2010; Wing et al., 2018). Statistical, machine-learning, and remote-sensing-based flood mapping approaches offer broader spatial coverage but depend on extensive historical flood inventories or sufficiently long satellite records, and often struggle to capture short-duration, pluvial, and drainage-related urban flooding, particularly where informal infrastructure dominates.

Against this backdrop, multi-criteria decision analysis (MCDA)–based relative flood risk mapping provides a pragmatic alternative by integrating multiple flood-contributing factors—such as topography, proximity to waterways, drainage density, soil properties, and land cover—into a transparent composite index representing relative susceptibility rather than absolute flood probability (Tehrany et al., 2014; de Moel et al., 2015). By relying on globally available geospatial datasets and expert-informed weighting schemes, MCDA approaches are computationally lightweight, interpretable, and transferable, making them well suited for early-stage flood risk screening and spatial prioritization in data-limited urban environments across Sub-Saharan Africa (Abebe et al., 2018; Ouma & Tateishi, 2014).

This work presents a GIS-based flood risk assessment framework that combines physical proximity to waterways, drainage network characteristics, soil infiltration potential, and land cover properties into a unified, raster-based flood risk index. By leveraging globally available geospatial datasets and open-source tools, the framework is designed to be transferable, computationally efficient, and applicable in data-constrained urban contexts. Rather than predicting event-specific inundation extents, the resulting index provides a comparative spatial representation of flood susceptibility that can support early-stage planning, infrastructure prioritization, and targeted risk reduction efforts in rapidly urbanizing regions of Sub-Saharan Africa.

2. Data and Methods

In this work, flood risk was evaluated using a raster-based multi-criteria framework in which several hydrologically-relevant spatial criteria were integrated on a common analysis grid. All input datasets were resampled to a common spatial resolution and co-registered to the same grid, ensuring that each raster cell represents the same geographic location across layers. This alignment enables direct pixel-wise comparison and weighted aggregation, producing a continuous flood risk surface over the study area.

The four primary criteria/data layers representing key physical controls on surface flooding that were used to derive the flood risk index are:

(i) proximity to rivers, drains, and channels, where shorter distances imply greater exposure to overbank flow and drainage overflow;

(ii) drainage network density, used as a proxy for surface runoff concentration and local hydrological connectivity;

(iii) soil infiltration potential, approximated using soil sand fraction, with higher sand content indicating greater infiltration capacity and reduced flood risk; and

(iv) land cover characteristics, reflecting differences in surface runoff, storage, and permeability between water bodies, wetlands, built-up areas, and vegetated surfaces.

Figure 1 and Sections 2.1 to 2.6 respectively present a block diagram and short descriptions of how these factors are incorporated into the method for flood risk estimation.

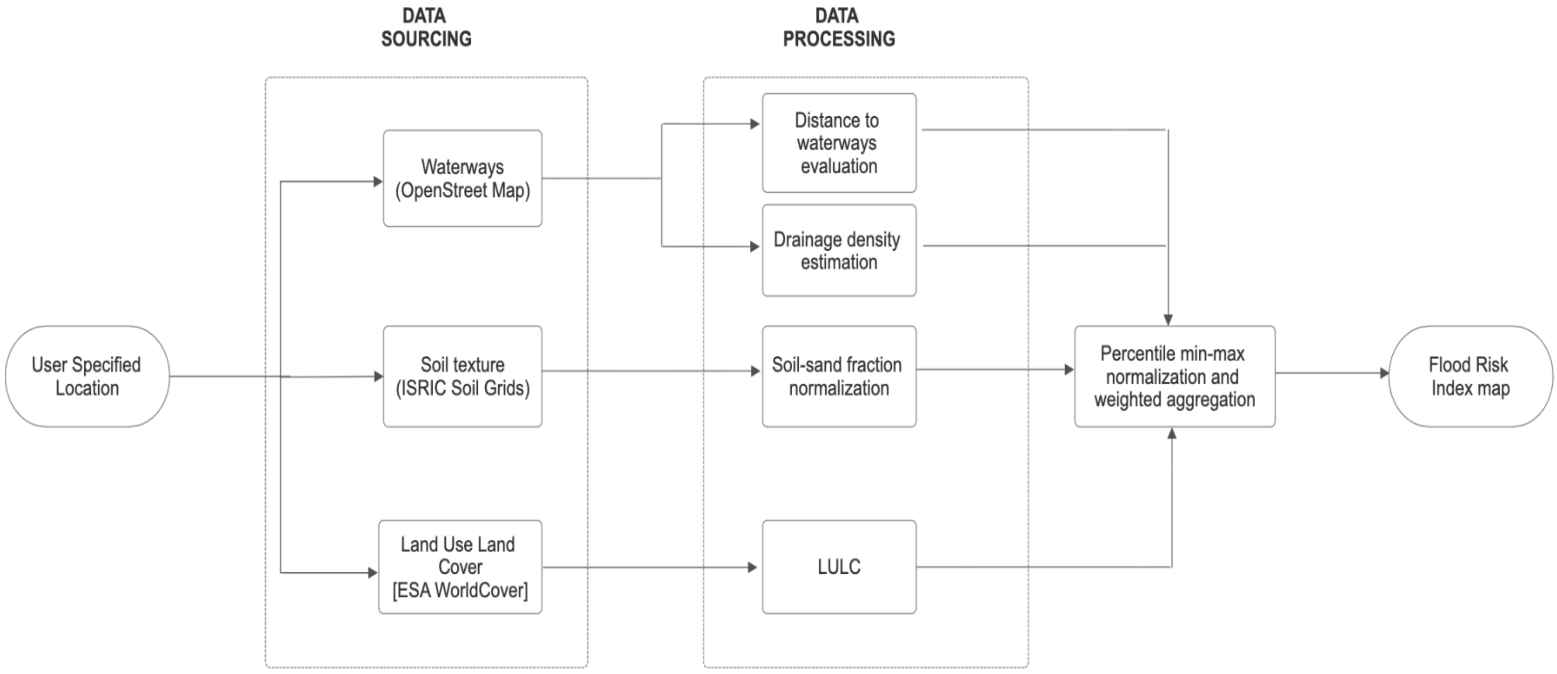

Figure 1: GIS-based Flood risk index methodology

2.1 Study Area Definition and Spatial Framework

For a user-specified administrative boundary under consideration (e.g. Lagos, Nigeria), a bounding box derived from OpenStreetMap is specified. A uniform raster grid is then generated over the area of interest, ensuring that all subsequent spatial datasets are resampled and aligned to a common spatial resolution and coordinate reference system. This grid serves as the analytical foundation for pixel-wise flood risk assessment.

2.2 Distance to Waterways

Proximity to surface water features was quantified using a distance-to-waterways raster, which captures the influence of rivers, channels, and standing water bodies on flood susceptibility. Vector representations of linear drainage features - including rivers, streams, canals, and engineered drains - were extracted from **OpenStreetMap** using standardized waterway=* tags. To account for flood-prone areas not represented by linear features alone, polygonal inland water bodies (e.g., lakes, reservoirs, wetlands, and permanent surface water) were also included. All water-related geometries were merged and rasterized onto a common analysis grid at the target spatial resolution, producing a binary water mask.

A Euclidean distance transform was applied to the water mask to compute the minimum distance from each grid cell to the nearest mapped water feature. For each raster cell , the distance-to-water value D_i is defined as:

$$D_i = \min_{j \in \mathcal{W}} d(i, j),$$

where $\mathcal{W}$ denotes the set of raster cells intersecting water features and $d(i, j)$ is the Euclidean distance between cell centers. Distances were converted from pixel units to meters using a latitude-adjusted degrees-to-meters conversion, and cells intersecting water features were assigned a distance of zero. Proximity to waterways is a well-established indicator of flood susceptibility, reflecting exposure to channel overtopping, backwater effects, and localized inundation along drainage corridors, particularly in urban and low-lying environments (Merz et al., 2007; Wing et al., 2018).

Figure 2 shows some example distance to waterways rasters for Lagos, Nigeria.

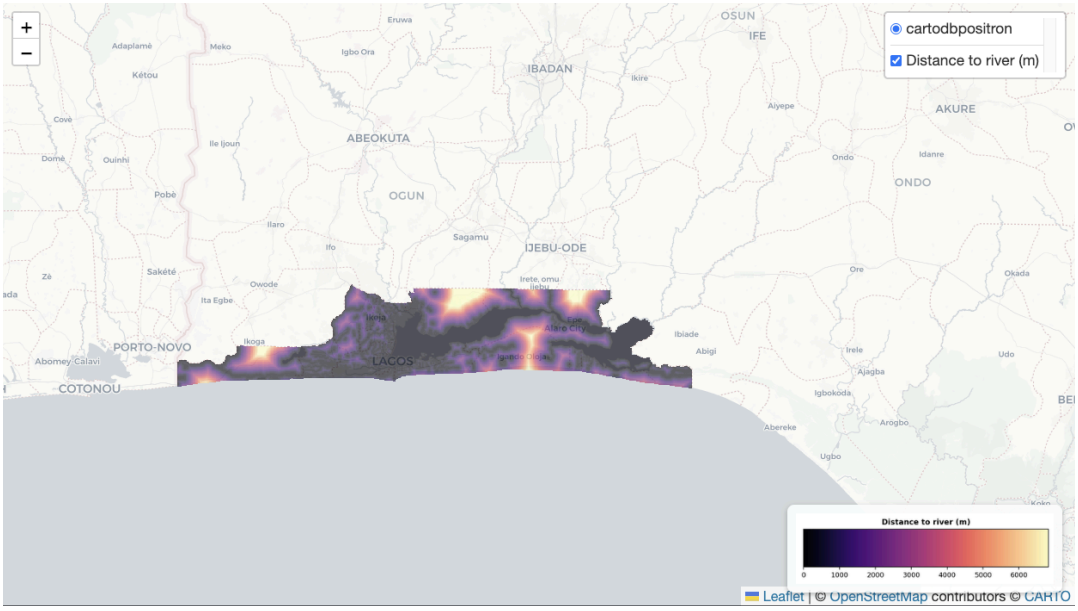

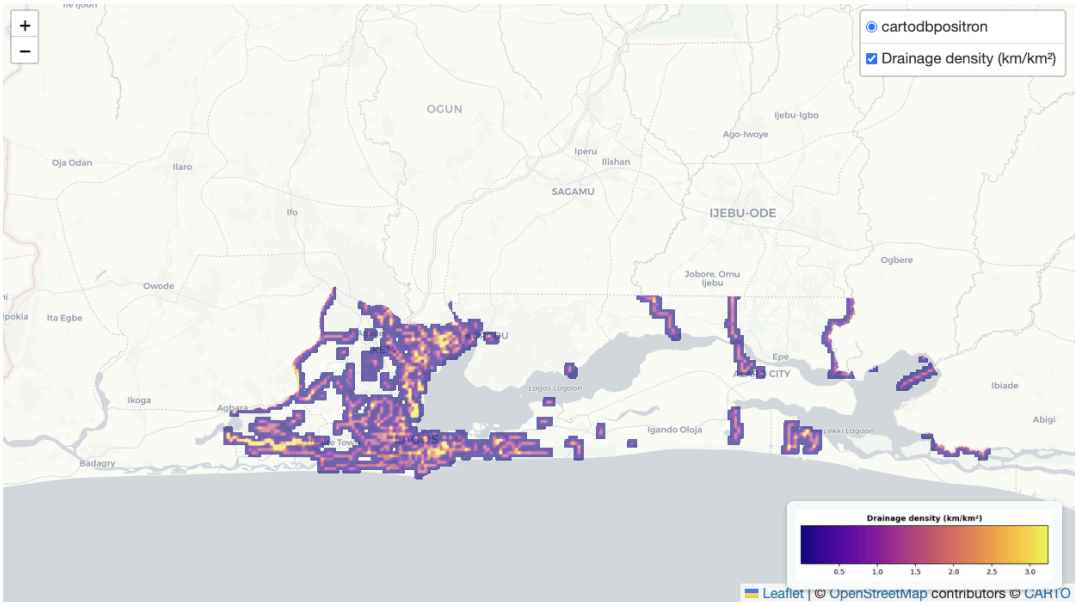

Figure 2: Distance to waterbodies raster (top) and Drainage density raster (bottom) Accra, Ghana

2.3 Drainage Density

Drainage capacity was approximated using a drainage density raster derived from the spatial concentration of mapped surface drainage channels. The OpenStreetMap waterway network was projected into a metric coordinate system to enable accurate length calculations. A regular fishnet grid was constructed over the area of interest, and within each grid cell k, the total length of drainage channels was summed and normalized by the cell area to yield drainage density values:

$$\rho_k = \frac{L_k}{A_k}$$

where L_k is the total channel length within cell k and A_k is the corresponding cell area. Drainage density values were expressed in kilometers of channel per square kilometer and rasterized onto the common analysis grid to ensure spatial alignment with other flood-related indicators. To reduce block artifacts arising from discrete grid aggregation and uneven mapping density, a light spatial smoothing filter was applied.

In urban environments and adjacent urban–rural transition zones, drainage density serves as a proxy for runoff concentration potential and the structural complexity of the drainage

network. Areas with high drainage density often coincide with low-relief terrain, engineered drainage corridors, or historically flood-prone zones where surface runoff is rapidly conveyed and concentrated during intense rainfall events. While dense drainage networks may enhance conveyance under moderate conditions, they can also exacerbate flooding during extreme storms when channel capacity is exceeded or drainage infrastructure becomes surcharged (O'Driscoll et al., 2010; Di Baldassarre et al., 2017). Accordingly, drainage density is interpreted here as an indicator of flood susceptibility rather than a direct measure of hydraulic performance.

Figure 2 shows an example of the generated drainage density rasters for Accra, Ghana.

2.4 Soil-Sand fraction (Soil infiltration Proxy)

Soil permeability was represented using a soil-sand fraction raster, which serves as a proxy for infiltration capacity and subsurface drainage behavior. Soil texture data were obtained from **ISRIC – World Soil Information** through the **SoilGrids** global soil property database. SoilGrids provides spatially continuous estimates of soil texture fractions derived from machine-learning models trained on a large compilation of in situ soil profiles and environmental covariates. In this study, the sand fraction for the upper soil layer (0–5 cm depth) was selected, as near-surface soil properties exert the strongest control on infiltration and initial runoff generation during rainfall events.

The SoilGrids sand fraction product was accessed via a Web Coverage Service (WCS), clipped to the buffered area of interest, and resampled to the common analysis grid using bilinear interpolation. The resulting raster represents the percentage of sand content by mass for each grid cell. To facilitate integration with other flood indicators, the sand fraction values were normalized to a continuous 0–1 scale, where higher values indicate greater infiltration potential and lower expected surface runoff.

Formally, the soil infiltration proxy S_i for grid cell i is defined as:

$$S_i = \frac{f_i^{\text{sand}} - f_{\text{min}}^{\text{sand}}}{f_{\text{max}}^{\text{sand}} - f_{\text{min}}^{\text{sand}}},$$

where f_i^{sand} is the sand fraction at cell i, *and* $f_{\text{min}}^{\text{sand}}$ and $f_{\text{max}}^{\text{sand}}$ are the minimum and maximum sand fraction values observed within the study area. In the composite flood risk calculation, this normalized proxy is inversely related to flood susceptibility, as higher sand content generally corresponds to higher hydraulic conductivity, faster percolation, and reduced surface runoff generation (Rawls et al., 1983; Schaap et al., 2001).

In urban areas and their surrounding urban-rural fringe zones - particularly in areas with partially impervious cover, compacted soils, or unpaved surfaces - soil texture exerts a secondary but non-negligible influence on flood susceptibility. Although urban development may significantly alter natural soil structure, sand fraction remains a useful screening-level indicator of relative infiltration potential in data-scarce regions. Consequently, the soil sand fraction layer is interpreted as a first-order proxy for infiltration capacity rather than a direct representation of effective hydraulic conductivity.

Figure 3 shows an example of the generated soil-sand ratio raster for Kinshasa, Democratic Republic of Congo.

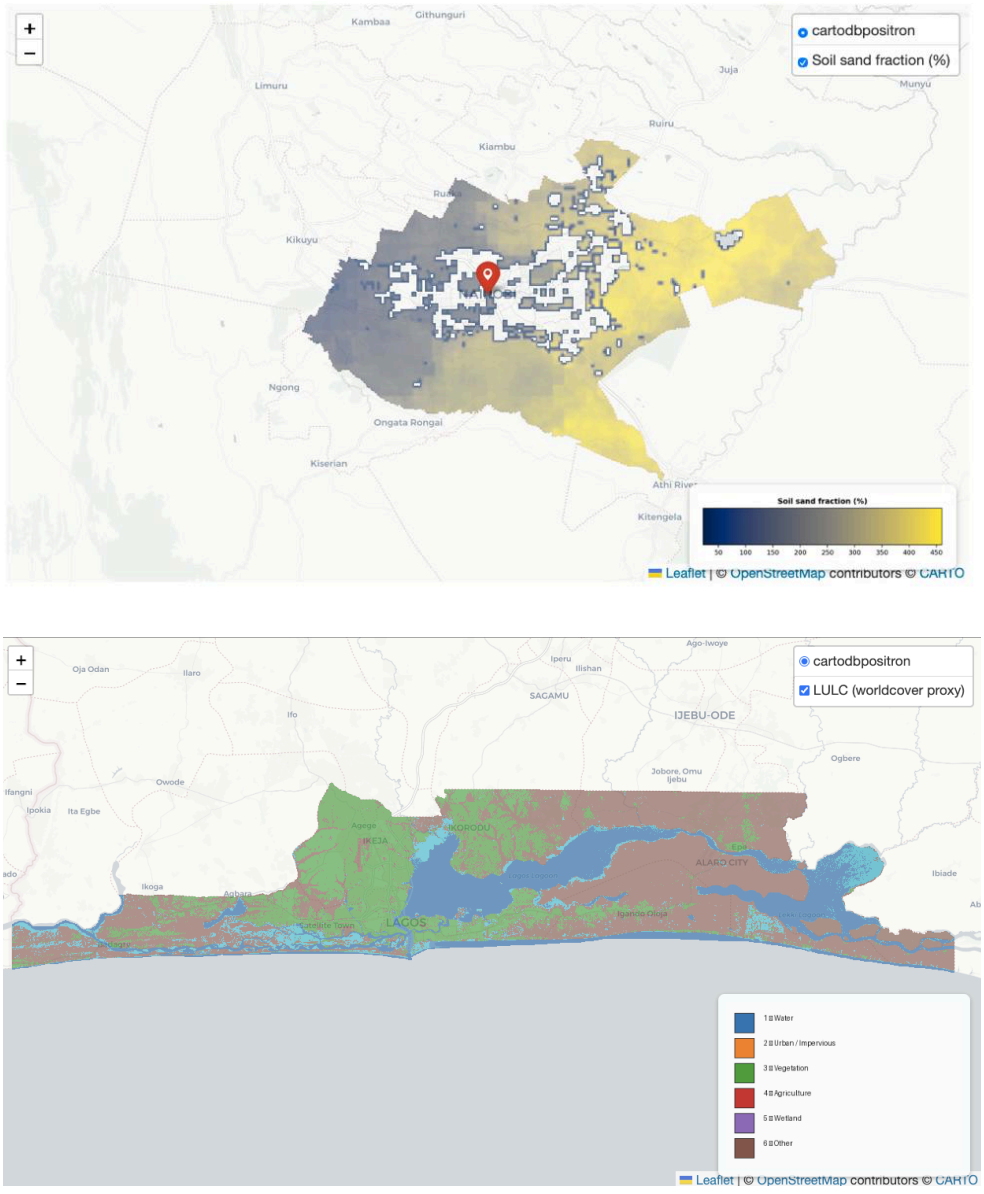

Figure 3: SoilGrids soil - sand ratio raster for Kinshasa, DRC (top) and ESA WorldCover LULC raster for Lagos, Nigeria (bottom)

2.5 Land Cover Classification

Land use and land cover (LULC) information was obtained from global, satellite-derived classification products accessed via the Microsoft Planetary Computer (Microsoft, 2023). The primary dataset used is **ESA WorldCover**, which provides a globally consistent land cover map at 10 m spatial resolution derived from Sentinel-1 and Sentinel-2 imagery using machine-learning classification techniques. WorldCover was selected as the primary source due to its high spatial detail, global coverage, and standardized legend.

In cases where WorldCover tiles were unavailable for the specified area of interest or acquisition year, the analysis automatically falls back to the **Impact Observatory Annual LULC dataset**, which also provides 10 m resolution global land cover maps derived from deep learning–based interpretation of multi-temporal Sentinel imagery. This fallback mechanism ensures continuity of data coverage while maintaining comparable spatial resolution and thematic content.

For each study area, all LULC tiles intersecting the buffered area of interest were queried, downloaded, and mosaicked into a single raster. The resulting mosaic was then reprojected and resampled onto the common analysis grid used by all flood-related indicators, ensuring pixel-level spatial alignment across datasets. Native land cover classes are reclassified into six generalized categories: water, built-up, vegetation, agriculture, wetland, and other. Each class is assigned a flood risk weight based on expected runoff behavior and water retention characteristics.

LULC datasets like the one sourced here are in practice land cover maps with some land-use inference. So a LULC “vegetation” actually means the land cover classifier sees green reflectance but the land use may be urban, informal, or industrial.

Figure 3 shows an example of the generated LULC raster for Lagos, Nigeria.

2.6 Normalization and Flood Risk Index Construction

All input layers are normalized to a common 0–1 scale using robust percentile-based min–max normalization to reduce the influence of outliers. For a layer X,

$$X_{norm} = (X - P_2(X))/(P_{98}(X) - P_2(X))$$

where $P_2(X)$ and $P_{98}(X)$ denote the 2nd and 98th percentiles, respectively. Values are clipped to the range [0,1].

Because MCDA aggregation assumes consistent directionality, mitigating layers are inverted so that higher normalized values uniformly correspond to higher flood susceptibility across all inputs. The final flood risk index (FSI) computed as a weighted linear combination of normalized indicators is:

$$FSI = w_d \cdot D + w_{dd} \cdot DD + w_s \cdot S + w_l \cdot L$$

where D is normalized distance-to-waterway risk, DD is normalized drainage density, S is normalized soil-related risk, L is land cover risk, and w denotes indicator weights. The resulting index is normalized again to ensure values lie between 0 and 1. This normalization places all contributing factors on a common scale and enables direct comparison between locations within the study area. Importantly, the index does **not** represent an absolute probability of flooding, expected inundation depth, or flood frequency; instead, it reflects **relative flood risk** based on the spatial co-occurrence of sourced flood-contributing conditions ie distance from waterways, drainage density, inferred infiltration capacity, and land cover types associated with runoff. A sample categorization of the relative flood risk of areas in a given flood risk map based on the index in those areas is [0.0 - 0.3], [0.3 - 0.7], [0.7 - 1.0] as low risk, moderate risk and high risk respectively.

3. Output and Discussion of results

The output of the model in this work is a raster that is a flood risk map, an example of which is shown in Figures 4 and 5 below. Presentation to the user is natively done via a Streamlit Graphical User Interface (GUI).. The Streamlit interface enables interactive exploration of the flood risk index and its component layers in a transparent and user-friendly manner. The main map displays the flood risk surface as a semi-transparent overlay on an interactive basemap, with controls for opacity and layer visibility, allowing users to inspect both the composite result and individual layer inputs. This design supports intuitive interpretation of model behavior and facilitates exploratory analysis and communication without the need for specialized GIS software. The areas of the map are rated with a FRI which is 0 to 1 continuous normalized unitless index where values closer to 1 indicate relatively higher susceptibility to flooding and values closer to 0 indicate relatively lower susceptibility.

To discuss the results of the model, consider Figure 5 above which shows the model output when applied to 2 different cities - Lagos, Nigeria and Accra, Ghana . The flood risk index reveals contrasting urban flood susceptibility patterns between Lagos and Accra, consistent with differences reported in recent news and secondary sources. In Lagos, elevated risk values are spatially extensive, spanning lagoon margins, coastal lowlands, and major drainage corridors across the metropolitan area. This pattern aligns with news reports which describe flooding as a citywide phenomenon during peak rainy seasons, driven by intense rainfall, blocked or undersized drainage infrastructure, informal development along waterways, and coastal backwater effects.

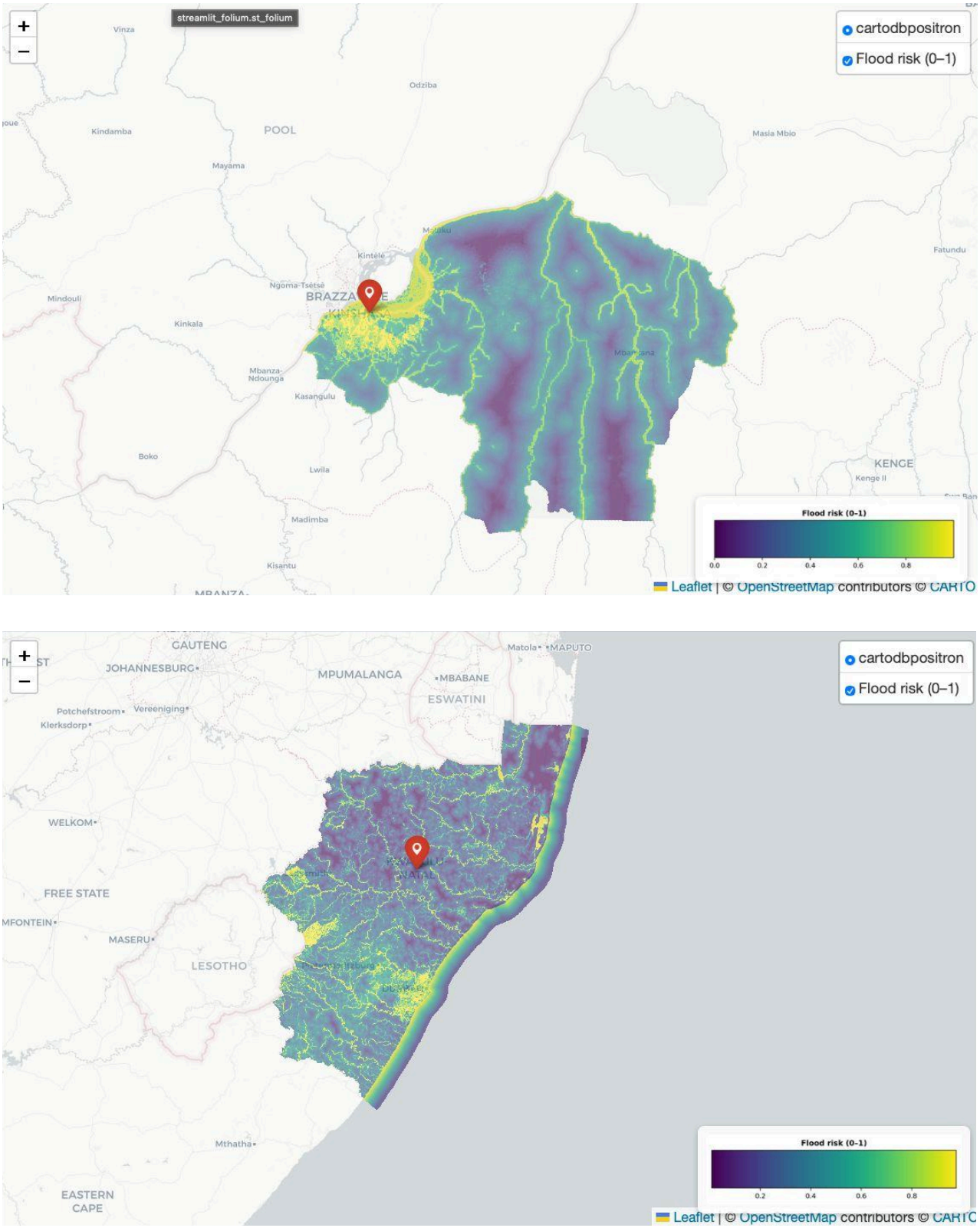

Figure 4: Flood risk index map for Kinshasa, Democratic Republic of Congo (top) and Durban, South Africa (bottom) using the model presented in this work.

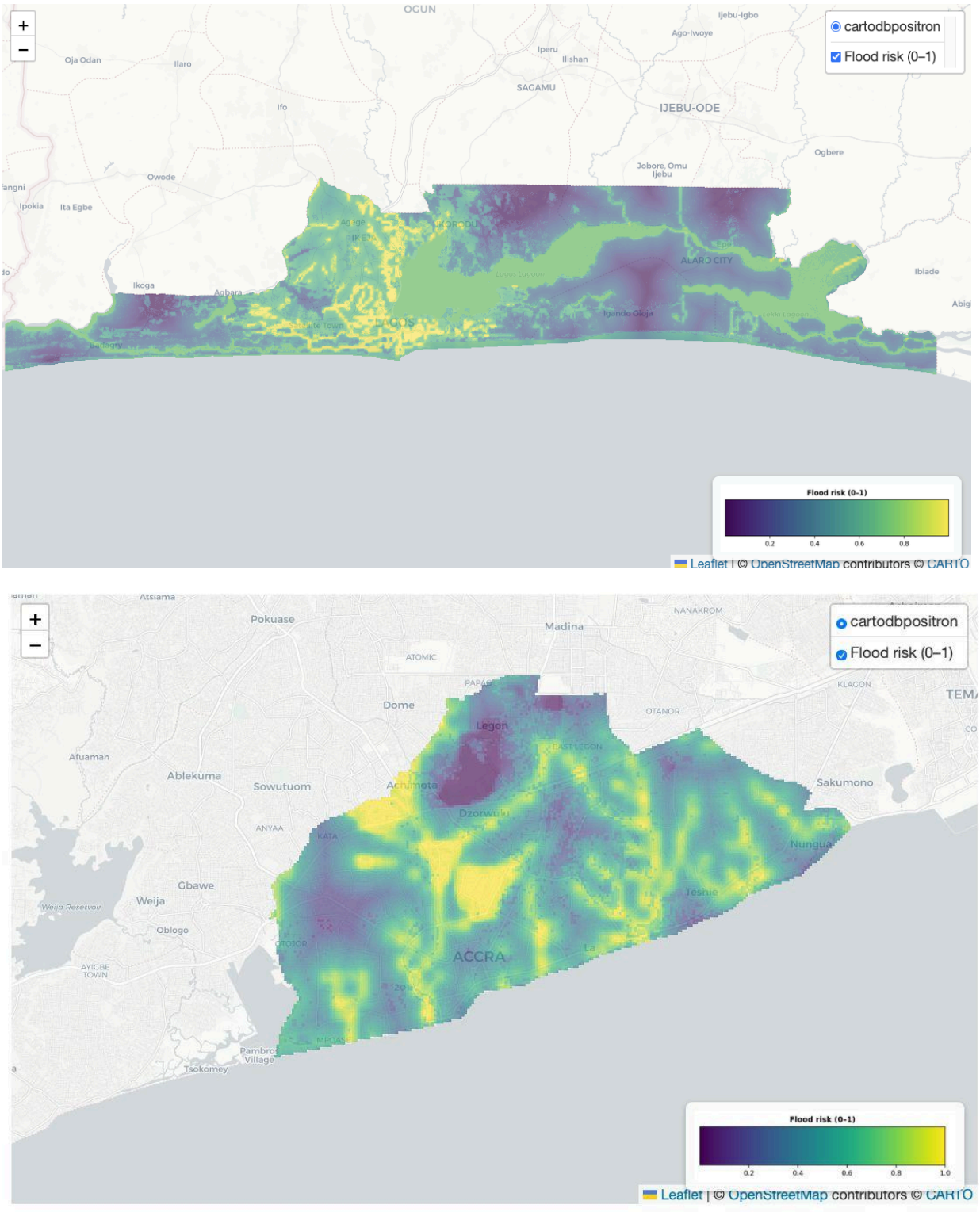

Figure 5: Flood risk index map for Lagos, Nigeria (top) and Accra, Ghana (bottom) using the model presented in this work.. Values range from 0 (lower relative flood susceptibility) to 1 (higher relative flood susceptibility) within the mapped area.

By contrast, the Accra flood risk map exhibits more spatially concentrated high-risk zones aligned with specific inland drainage basins and low-relief corridors. This mirrors news reporting which frequently characterizes flooding in Accra as severe but localized, resulting from short-duration, high-intensity rainfall overwhelming drainage channels and causing rapid runoff accumulation in downstream neighborhoods. Together, these contrasting patterns suggest that flooding in Lagos is governed by a compound coastal–urban flood regime with widespread exposure, whereas flooding in Accra is more strongly controlled by basin-scale drainage bottlenecks and pluvial processes. The flood risk index reproduces these observed differences without event-specific hydrodynamic modeling, supporting its use as a comparative, screening-level tool for urban flood susceptibility assessment.

The interactive web-based user interface, built with Streamlit and Folium, provides a comprehensive flood risk visualization and analysis platform that enables real-time risk assessment through dynamic parameter adjustment and multi-source data integration. The interface features:

- Interactive point queries: Location search with geocoding, sampled raster values at markers, and automatic map recentering.
- Interactive map visualization: Five toggleable geospatial layers with scientific colormaps, semi-transparent overlays, and dynamically positioned legends.
- Configurable risk computation: Sidebar weight sliders for four input layers that support location re-fetching or weight-only recomputation.
- Meteorological integration: 7-day rainfall forecasts with risk-adaptive thresholds, styled tables with weather icons, and probability metrics.
- Historical rainfall analysis: Quarterly NASA POWER precipitation data shown as stacked bar charts across multiple years to facilitate context inference for a given location.
- Spatial risk interpretation: Automated high-risk subregion identification with optional AI-generated or rule-based explanations.
- Smart session management: Stateful caching tracking AOI changes to prevent unnecessary refetching while maintaining responsiveness

4. Conclusion - summary, limitations and future improvements

The open-source framework presented in this work is an easy-to-adapt platform for evaluating flood-risk in a given geographical area using surface properties (distance to waterways, drainage density, soil infiltration and LULC) from openly available data. The resulting flood risk index is a spatial comparative measure of the likelihood of flooding of sub-areas in a particular area of interest. The results are natively presented in a Streamlit GUI and thus the whole framework facilitates accessible and easy-to-adapt flood evaluation without the need for proprietary data.

While there is an indication of the rainfall expectation in the evaluated area based on historical trends, screening-level assessment does not explicitly model flood depths, flow velocities, or flood return periods. Indicator weights are based on user judgment rather than empirical calibration, which may introduce subjectivity. Input datasets such as OpenStreetMap and global soil products vary in spatial accuracy and completeness across regions. Additionally, dynamic processes such as rainfall intensity, storm duration, and drainage capacity are not explicitly represented.

While this work is good for comparative spatial flood risk assessment under data constraints, the presented framework does not explicitly simulate flood depths, flow velocities, or return periods that would be available in a detailed hydrodynamic model. To partially address this limitation in Sub-Saharan environments, the framework can be extended through the incorporation of simplified rainfall intensity proxies (e.g., satellite-derived extreme rainfall climatologies), event-based scenario layers, or locally derived empirical flood observations where available. Another limitation of this work is that layer aggregation weights are currently based on subjective user/expert judgment rather than empirical calibration. This can be mitigated through sensitivity analysis, participatory weighting with local planners and engineers, or calibration against documented historical flood extents derived from satellite imagery.

Input datasets such as OpenStreetMap and global soil products vary in spatial accuracy and completeness across regions, particularly where informal drainage networks are underrepresented. This limitation may be reduced through local validation, integration of community-mapped data, or incorporation of higher-resolution national datasets when available. Machine learning based image processing methods could also improve this estimation. Another future enhancement is the incorporation of remotely sensed rainfall products, simplified runoff coefficients differentiated by land cover, or drainage density refinement using locally mapped infrastructure to better reflect urban hydrological behavior while maintaining computational efficiency.

While the work includes an interactive, adaptable graphical GUI via Streamlit with adjustable opacity, possible improvements to the provided GUI includes suggestion-assisted location search, accepting user-provided shapefile/polygon input and provision of area evaluation report and downloadable rasters.

The Github Repo is open source and available at
https://github.com/OpenSourceCollective/flood_risk

5. Acknowledgement

The authors are members of Axum AI (https://axumai.org/), a collective whose objective is creating open-source solutions to address Africa's unique challenges. We acknowledge WeCollect and other members of Axum AI for their support in carrying out this work.

6. References

- Abebe, Y. A., Kabir, G., & Tesfamariam, S. (2018). *Assessing urban flood risk using GIS-based multi-criteria decision analysis*. Journal of Hydrology, 564, 1–13.

- Adelekan, I. O. (2016). *Flood risk management in the coastal city of Lagos, Nigeria*. Journal of Flood Risk Management, 9(3), 255–264.

- de Moel, H., van Alphen, J., & Aerts, J. C. J. H. (2015). *Flood maps in Europe – methods, availability and use*. Natural Hazards and Earth System Sciences, 9, 289–301.

- Di Baldassarre, G., Viglione, A., Carr, G., Kuil, L., Salinas, J. L., & Blöschl, G. (2017). *Socio-hydrology: Conceptualising human–flood interactions*. Hydrology and Earth System Sciences, 21, 477–493.

- Douglas, I., et al. (2008). *Unjust waters: Climate change, flooding and the urban poor in Africa*. Environment and Urbanization, 20(1), 187–205.

- IPCC. (2022). *Climate Change 2022: Impacts, Adaptation and Vulnerability*. Cambridge University Press.

- Merz, B., Hall, J., Disse, M., & Schumann, A. (2010). *Fluvial flood risk management in a changing world*. Natural Hazards and Earth System Sciences, 10, 509–527.

- Ouma, Y. O., & Tateishi, R. (2014). *Urban flood vulnerability and risk mapping using integrated multi-parametric AHP and GIS*. International Journal of Disaster Risk Reduction, 9, 150–165.

- Tehrany, M. S., Pradhan, B., & Jebur, M. N. (2014). *Flood susceptibility mapping using ensemble MCDA models*. Journal of Hydrology, 512, 332–343.

- Wing, O. E. J., et al. (2018). *Estimates of present and future flood risk*. Environmental Research Letters, 13(3), 034023.

- Merz, B., Thieken, A. H., & Gocht, M. (2007). *Flood risk mapping at the local scale: Concepts and challenges*. Flood Risk Management, 1(1), 1–15.

- O'Driscoll, M., Clinton, S., Jefferson, A., Manda, A., & McMillan, S. (2010). *Urbanization effects on watershed hydrology and in-stream processes*. Water, 2(3), 605–648.

- Zanaga, D., et al. (2021). *ESA WorldCover 10 m 2020 v100*. European Space Agency.

- Brown, C. F., et al. (2022). *Dynamic World, Near Real-Time Global 10 m Land Use Land Cover Mapping*. Scientific Data.

- Microsoft (2023). *Planetary Computer: A cloud-based platform for global-scale geospatial analysis*.